Rock Mechanics and Rock Engineering (2022) 55:2711–2728
https://doi.org/10.1007/s00603-021-02513-z

ORIGINAL PAPER

Material Properties and Triggering Mechanisms of an Andesitic Lava Dome Collapse at Shiveluch Volcano, Kamchatka, Russia, Revealed Using the Finite Element Method

Cory S. Wallace[1] · **Lauren N. Schaefer**[2] · **Marlène C. Villeneuve**[3]

Received: 17 December 2020 / Accepted: 19 May 2021 / Published online: 1 June 2021

Abstract

Shiveluch volcano (Kamchatka, Russia) is an active andesitic volcano with a history of explosive activity, dome extrusion, and structural collapse during the Holocene. The most recent major (> 1 km^3) dome collapse occurred in November 1964, producing a ~ 1.5 km^3 debris avalanche that traveled over 15 km from the vent and triggered a phreatic explosion followed by a voluminous (~ 0.8 km^3) eruption of juvenile pyroclastic material. Seismic records suggest that the collapse was likely triggered by a magnitude 5.1 earthquake associated with the ascent of magma into the edifice. The geomechanical properties of the pre-1964 dome are unknown; accordingly, the mechanics of the collapse are poorly understood. This project employs numerical slope stability modeling using the finite element method to constrain probable ranges of geomechanical properties for the materials involved in the collapse, considering earthquake loading as the most likely triggering mechanism. Model results show good agreement with the 1964 collapse geometry considering Geological Strength Index and horizontal pseudo-static seismic coefficient ranges of 30–60 and 0.05–0.15 g, respectively, representing variably fractured and altered dome rocks under moderate earthquake loading, confirming that ground acceleration alone could have triggered the dome collapse. Deep-seated rotational sliding is the dominant failure mode, but local extension within the dome during failure appears to play an important role in the development of the collapse. The findings of this work allow for better forward modeling of potential future collapses, the results of which can be incorporated into regional hazard and risk assessments.

Keywords Volcanic hazards · Debris avalanche · Lava dome · Collapse · Shiveluch

1 Introduction

Lava domes are accumulations of viscous lava that develop at shallow depths on the flanks and tops of volcanoes. Lava domes can be actively growing and/or cooling as hot, viscous lava intrudes through cooler fractured lava. They tend to evolve dynamically and develop highly fractured and oversteepened sides, making them prone to collapse as lava is emplaced. Due to their large volumes, lava dome failures can run out many kilometers from the volcanic edifice and reach populated areas, causing destruction of property and loss of life [e.g., Mt. Unzen, 1991–1994 (Ui et al. 1999)]. In addition, failure of lava domes, especially when at high temperature, can generate extremely destructive block-and-ash flows and lahars (Carn et al. 2004; Coats et al. 2018). Depressurization of hydrothermal and/or magmatic systems within lava domes or in volcanic edifices due to lava dome failure can trigger violent explosive activity [e.g., Mount St. Helens, 1980 (Voight et al. 1983)]. Lava domes become preconditioned to collapse due to oversteepening during extrusion (Diefenbach et al. 2013; Ashwell et al. 2018). Triggers of instability can include internal overpressures associated with pressurized gases (Voight and Elsworth 2000), magma (Schaefer et al. 2013), and/or hydrothermal fluids (Reid 2004); earthquake swarms (Calder et al. 2002); heavy rainfall (Carn et al. 2004); and changes in the rate or style of extrusion (Loughlin et al. 2010; Carr et al. 2016).

✉ Cory S. Wallace
cswallace@alumni.mines.edu

[1] Department of Geology and Geological Engineering, Colorado School of Mines, Golden, CO, USA

[2] U.S. Geological Survey, Geologic Hazards Science Center, Golden, CO, USA

[3] Chair of Subsurface Engineering, Montanuniversität Leoben, Leoben, Austria

Shiveluch volcano (Kamchatka, Russia) is an active andesitic stratovolcano that has experienced rapid lava dome growth and collapse throughout the Holocene (Belousov 1995; Ponomareva et al. 1998; Krippner et al. 2018). The most recent major (> 1 km^3) dome collapse occurred on 12 November 1964, producing a ~ 1.5 km^3 debris avalanche that traveled over 15 km from the vent and left a ~ 1.7-km-diameter horseshoe-shaped crater in the edifice (Belousov 1995). The collapse was preceded by a swarm of earthquakes, immediately followed by a phreatic explosion, and later followed by a voluminous (~ 0.8 km^3) eruption of juvenile pyroclastic material (Belousov 1995). The phreatic explosion following the 1964 collapse at Shiveluch suggests that a pressurized hydrothermal system existed within the edifice, and a delayed onset of Plinian activity suggests that magma had not intruded into the shallow edifice at the time of failure. Seismic records suggest that earthquake loading was a likely trigger (Belousov 1995; Gorelchik et al. 1997); the potential influence of elevated hydrothermal and/or fluid pressures as triggering mechanisms is unclear.

The rocks involved in the collapse and the associated debris avalanche deposits have been described in terms of their origin and emplacement mechanisms, but their physical and mechanical properties have not been characterized; therefore, the mechanics of the 1964 dome collapse at Shiveluch are poorly understood. To better understand the mechanics of the collapse, the geomechanical properties of the materials involved must be constrained, as they can have strong controls over failure behavior and failure mode (Reid et al. 2001, 2010; Lavallée and Kendrick 2021). Constraining these material properties represents an important step in developing volcanic stability evaluations and hazard assessments.

Slope stability models are useful for elucidating the mechanics of major collapse events and evaluating the sensitivity of slopes to changes in material properties and external loading when they cannot be determined otherwise. Continuum methods are typically used in geomechanical modeling when the degree of fracturing in the rock is high relative to the scale of the terrain, such that the rock mass can be represented by an equivalent continuum (Sitharam et al. 2001; Hammah et al. 2005). Researchers have evaluated volcano flank and edifice stability using continuum approaches such as limit equilibrium methods (LEM) (Iverson 1995; Schaefer et al. 2013, 2018), finite element methods (FEM) (Sousa and Voight 1995; Schaefer et al. 2013), and finite difference methods (FDM) (Hürlimann et al. 2000; Apuani et al. 2005a). Numerical methods such as FEM and FDM are particularly effective for evaluating failure modes by identifying concentrations of stresses and strains in the rock mass at the onset of instability (Hammah et al. 2005) based on slope geometry and generalized subsurface conditions. In this study, we employ FEM to constrain probable ranges of geomechanical properties for the materials involved in the 1964 edifice collapse at Shiveluch, considering seismic loading as the most likely triggering mechanism. Based on deposit descriptions, we use a range of materials, from fresh to extensively altered, to represent the dome rocks. We determine geomechanical properties for analogue andesite samples using uniaxial and triaxial compressive strength laboratory tests. We then examine how rock mass quality and alteration can influence failure mode and highlight broader implications for volcanic hazards.

2 Geographic and Geologic Setting

Shiveluch is located on the Kamchatka peninsula within the Central Kamchatka Depression, a ~ 150-km wide, low-lying plain between the Sredinny range to the west and the Vostochny range to the east (Fig. 1a). The Kamchatka peninsula is situated at the junction of the Kuril-Kamchatka and Aleutian subduction zones, where the Pacific plate is subducting to the west beneath the Okhotsk plate (Seno et al. 1996; Krippner et al. 2018). Shiveluch is the northernmost active volcano on the Kamchatka peninsula and is one of the most active volcanoes in the region with an average magma discharge of ~ 0.015 km^3/year (Ponomareva et al. 2007). The Holocene eruptive history of Shiveluch is characterized by alternating periods of explosive activity and dome growth, separated by periods of quiescence, with the most recent voluminous eruptive period beginning around 900 BCE (Ponomareva et al. 2007).

The Shiveluch edifice is composed of two parts: an older, inactive, primary summit (Old Shiveluch) and a younger, active, subsidiary summit (Young Shiveluch) (Fig. 1b). Old Shiveluch (summit elevation 3307 m above sea level [asl]) is a remnant of a large stratovolcano that collapsed catastrophically during the late Pleistocene, forming a ~ 10 km^3 debris avalanche and leaving a collapse caldera ~ 9 km across, opening to the south (Belousov 1995; Ponomareva et al. 1998). Young Shiveluch (pre-1964 summit elevation ~ 2800 m asl) consists of multiple coalesced extrusive lava domes that formed within the late Pleistocene collapse scar (Ponomareva et al. 1998).

Old Shiveluch is composed primarily of andesite and basaltic andesite flows and domes (Belousov 1995). The volcano was constructed during the late Pleistocene in two stages: an earlier pyroclastic stage and a later effusive stage; as such, sequences of lava flows in the upper portion of the volcano generally overlie pyroclastic deposits in the lower portion (Gorbach et al. 2013). The massive late Pleistocene collapse scar exposes hydrothermally altered lavas and pyroclastic deposits through which the andesitic domes of Young Shiveluch are extruded (Gorbach et al. 2013). Volcanic collapses and subsequent debris avalanches have occurred

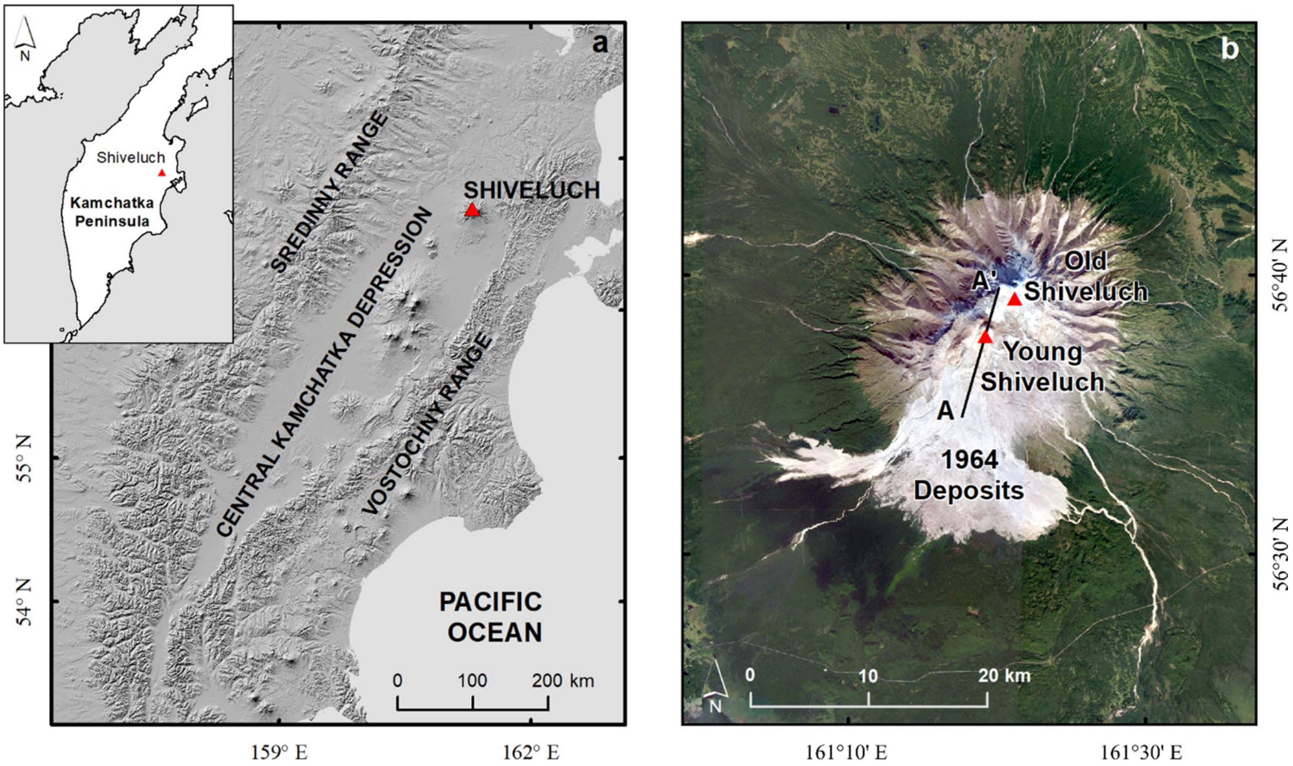

Fig. 1 **a** Location of Shiveluch on the Kamchatka peninsula of eastern Russia. Shaded relief map is based on 90 m SRTM digital elevation data obtained from CGIAR-CSI (available at http://srtm.csi.cgiar.org). **b** Satellite image of Shiveluch volcano showing the older, primary summit (Old Shiveluch), the younger, subsidiary summit (Young Shivluch), and the debris avalanche deposits associated with the 1964 collapse of Young Shiveluch. Image source: Landsat/Copernicus (downloaded from Google Earth). Image date: September 2013

repeatedly at Young Shiveluch throughout the late Holocene, with at least 13 collapses preceding the 1964 event in the last 5.7 ka (Ponomareva et al. 1998).

3 November 1964 Collapse Sequence

Earthquake activity associated with the 1964 collapse of Shiveluch commenced in January 1964, with notable earthquake swarms occurring in early May and late October 1964 (Bogoyavlenskaya et al. 1985; Belousov 1995). In the early morning of 12 November 1964, a swarm of at least 70 shallow (0–40 km deep) earthquakes (Gorelchik et al. 1997) occurred at Shiveluch, producing nearly constant ground shaking. The strongest (M 5.1) earthquake occurred less than 10 km deep directly under Shiveluch at 07:07 (Belousov 1995; Gorelchik et al. 1997; Gusev et al. 1998). Gorelchik et al. (1997) generally associate these shallow earthquakes with lava dome activity in the central part of the edifice, and Belousov (1995) concludes that the M ~ 5 earthquake preceding collapse was associated with magma ascent into the edifice. This earthquake immediately preceded the collapse of the dome, initiating a ~ 1.5 km^3 debris avalanche that traveled over 15 km to the south–southwest, blanketing much of the southern flank of Shiveluch with debris (Belousov 1995). The collapse depressurized a hydrothermal system within the edifice, causing a phreatic explosion. Air waves recorded at 07:07 at nearby meteorological stations confirm the nearly simultaneous onset of explosive activity following the earthquake and dome collapse (Gorshkov and Dubik 1970). A sharp increase in air wave energy was recorded at 07:20 as the first juvenile magmatic material was explosively erupted, generating pyroclastic flows (Gorshkov and Dubik 1970; Belousov 1995). Plinian-style activity continued until the eruption ceased at 08:22. Studies of the new deposits several days after the eruption showed that the debris avalanche did not include any juvenile magmatic material; rather, the voluminous (~ 0.8 km^3) outpouring of juvenile pyroclastic material initiated after the collapse had occurred (Belousov 1995). The delay between the edifice collapse at 07:07 and the onset of Plinian activity at 07:20 suggests that magma had not intruded into the shallow edifice at the time of the collapse, and, therefore, probably was not an immediate trigger of instability (Belousov 1995), although the intrusion of magma deeper in the edifice could have led to deformation or oversteepening at the surface, which could have preconditioned the edifice for collapse (similar to that observed at Mount St. Helens, 1980 Lipman et al. 1981; Voight et al. 1983). The phreatic explosion suggests that hydrothermal pressures were present in the edifice, but whether these pressures were a preconditioning factor for collapse remains uncertain. Based on this sequence of events, earthquake loading associated with the ascent of magma appears to be the most probable trigger of the collapse (Belousov 1995); thus, we explore this triggering mechanism by modeling the collapse under moderate (M ~ 5) earthquake loading.

4 Materials

The rocks and debris avalanche deposits at Young Shiveluch have been described in terms of their origin and emplacement mechanisms (Gorshkov and Dubik 1970; Bogoyavlenskaya et al. 1985; Belousov 1995; Ponomareva et al. 1998; Gorbach et al. 2013), but no work has been done to characterize their geomechanical properties. Here, we synthesize key descriptions of the dome rocks at Young Shiveluch based on descriptions of intact blocks within the 1964 debris avalanche deposits. We correlate these descriptions with the results of recent geotechnical testing of representative andesitic rocks collected from Mt. Ruapehu (Taupo volcanic zone, North Island, New Zealand), an active stratovolcano that is compositionally similar to Shiveluch, to assemble likely ranges for geomechanical properties of the Shiveluch dome materials.

4.1 Shiveluch 1964 Debris Avalanche Deposit Descriptions

Bogoyavlenskaya et al. (1985) describe the deposits of the 1964 collapse as poorly sorted, poorly stratified agglomerate containing large rock fragments and debris of the old edifice, which consist of gray to pink andesites ranging from dense to pumiceous. This suggests that the composition of the pre-1964 edifice was primarily andesitic lava with highly variable porosity. Belousov (1995) describes intact blocks in the debris avalanche deposits as being unaltered to extensively altered, with gypsum-bearing blocks up to 0.5 m in diameter, which suggests that the alteration of the dome rock is locally extensive but not necessarily pervasive throughout the edifice.

4.2 Representative Mechanical Properties of Andesitic Rocks

Based on descriptions of the Shiveluch debris avalanche deposit, we modeled the dome using mechanical properties representative of typical andesite ranging from unaltered to pervasively altered. Altered lava can be significantly weaker than fresh lava due to replacement of strong minerals by weaker minerals such as clays (Reid et al. 2001; Ball et al. 2015). Altered material at depth has been shown to have different physical properties than that at the surface due to clay precipitation into cracks and pores (Siratovich et al. 2016); therefore, we also considered typical properties of a pervasively altered subsurface andesite. We selected three blocks of andesite fitting these descriptions from a collection of lava samples from the active andesitic Mt. Ruapehu volcano. This volcano has an active hydrothermal system and various materials exposed at the surface, ranging from fresh to extensively altered (Mordensky et al. 2018b). Selected samples included (1) Sample 1, a fresh block with minor surface weathering only; (2) Sample 2, a porous and moderately to pervasively altered (supergene argillic alteration) and weathered block; and (3) Sample 3, a pervasively altered (steam-heated, intermediate to advanced argillic alteration) block erupted from the 1995–1996 eruption representing the host rock beneath the current vent-hosted hydrothermal system (Fig. 2).

5 Methods

5.1 Laboratory Testing

Geomechanical data used as inputs for our numerical models include uniaxial compressive strength (UCS), Young's modulus (E), and the Hoek–Brown material constant m_i (an empirical material constant analogous to the frictional strength of the intact rock [Sari 2010; Eberhardt 2012; He

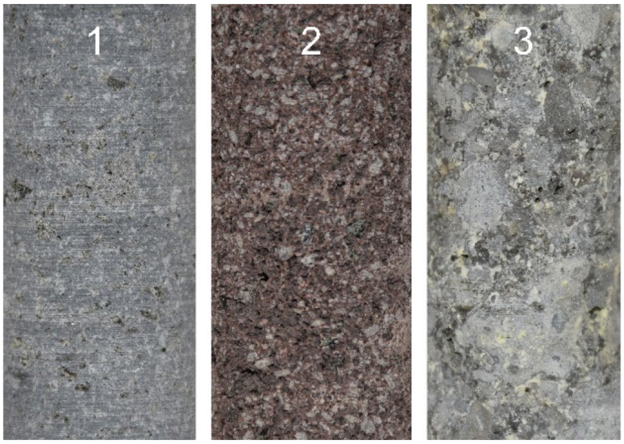

Fig. 2 Andesite blocks from Ruapehu volcano (New Zealand) used as analogue for the range of materials composing the Shiveluch dome based on descriptions of the debris avalanche deposit, including: (1) Sample 1, fresh, unaltered andesite (upper end member for strength); (2) Sample 2, a porous and moderately to pervasively altered (supergene argillic alteration) andesite (lower end member for strength); and (3) Sample 3, pervasively altered (steam-heated, intermediate to advanced argillic alteration) subsurface andesite (middle range for strength)

et al. 2020]) calculated from triaxial compressive tests at various confining pressures using the nonlinear generalized Hoek–Brown empirical failure criterion (Eberhardt 2012) in RocData software (RocScience 2019a). We measured UCS and triaxial strength using a Technotest 3000-kN servo-controlled loading frame at a constant strain rate of 1.0×10^{-5} s^{-1}. A minimum of six 20 mm diameter, 40 mm long, right cylindrical cores were prepared from each of the sample blocks described above: three for UCS testing and three for triaxial testing. Measurements were conducted on oven-dried samples at room temperature. UCS tends to increase as water content decreases through oven drying (Wong et al. 2016; Hashiba et al. 2019); as such, the UCS values obtained here may slightly overestimate the in situ rock strength conditions. Mean values from the three UCS tests were evaluated to produce one strength value and Young's modulus value for each block. Prior to testing, we determined the porosity for each core using a Micromeritics AccuPyc II 1340 helium pycnometer and averaged the results to produce one porosity value for each sample block.

5.2 Generalized Geological Cross Section

For slope stability modeling, we constructed a generalized geological cross section representing the topography and expected subsurface conditions of Young Shiveluch at the time of failure in 1964 (Fig. 3). The cross section shows the pre- and post-failure topography of the dome from Ponomareva et al. (1998) and shows the assumed failure surface based on the post-failure topography. The cross section corresponds to profile line A–A' in Fig. 1. Because the properties of the flanks and edifice of Old Shiveluch are unknown, the subsurface materials are assumed to be uniform and the same as the dome materials. This cross section is simplified to account for uncertainties associated with limited knowledge of site-specific geological conditions and is prepared for the purposes of slope stability modeling. The locations of the features depicted are approximate. We suspect that the failure surface at depth primarily crosses through altered materials, as suggested by the relatively extensive zone of hydrothermal alteration in Fig. 3.

5.3 Edifice Failure Models

We performed a series of slope stability analyses based on the geological cross section presented in Fig. 3., using the two-dimensional geotechnical finite element analysis program RS2 10.0 (RocScience 2019b). The model geometry and finite element mesh are shown in Fig. 4. The model

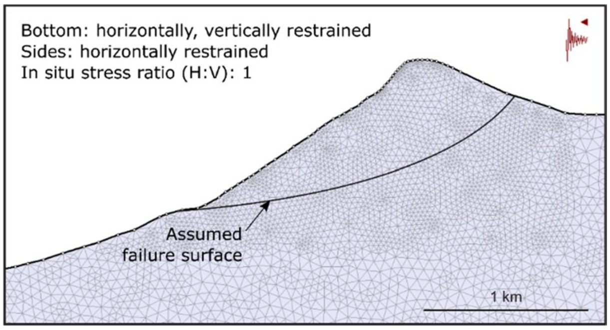

Fig. 4 RS2 model setup showing topography of Shiveluch edifice, finite element mesh, boundary conditions, in situ stress ratio (H:V), and direction of seismic force application (upper right)

Fig. 3 Generalized geological cross section along profile A–A' (Fig. 1). Topography is from Ponomareva et al. (1998) with no vertical exaggeration. Subsurface materials are assumed to be uniform and the same as the pre-1964 dome material. *YS* Young Shiveluch, *OS* Old Shiveluch, *LD* Pre-1964 lava dome, *PT* Post-1964 surface topography, *FS* Approximate failure surface (assumed based on post-1964 surface topography), *HA* Zone of hydrothermal alteration (shown schematically; extents are unknown)

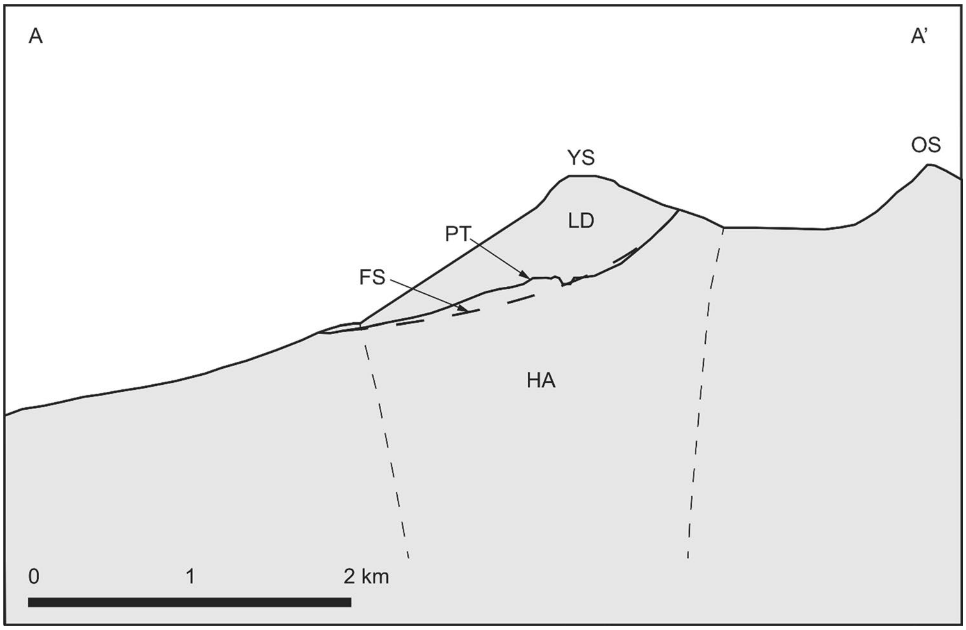

boundaries are restrained horizontally and vertically along the bottom of the model and horizontally along the sides.

These analyses used the Shear Strength Reduction method (Dawson et al. 1999; Hammah et al. 2005) to evaluate a critical strength reduction factor (SRF) for which the model reaches a stability threshold. The critical SRF is equivalent to the factor of safety against slope failure (Dawson et al. 1999) or the ratio of shear strength to shear stress required to maintain stability (Bishop 1955). We modeled the rock mass strength envelopes using the generalized Hoek–Brown strength criterion (Eberhardt 2012) based on the representative UCS and m_i values determined by our laboratory testing and back-calculated Geological Strength Index (GSI) values, which characterize the quality of the rock mass in terms of the degree of fracturing and the physical condition of discontinuities (Hoek et al. 2013; Bertuzzi et al. 2016). Rock mass elastic modulus values were evaluated using the generalized Hoek and Diederichs method (Hoek and Diederichs 2006) based on representative intact Young's modulus values and GSI values.

The goals of our modeling were to (1) constrain the rock mass strength parameters of the dome materials involved in the 1964 collapse at Shiveluch through back-calculation; (2) evaluate the likelihood of seismic loading as the predominant triggering mechanism; and (3) assess how changes to model input parameters affect the modeled failure mode. Using the mechanical properties of representative andesitic rocks determined through geotechnical testing as a baseline, our general modeling approach was to constrain a range of GSI values that allowed for the observed 1964 collapse to occur, given a moderate (M ~ 5) earthquake. To achieve this, we back-calculated GSI values corresponding to a critical SRF of 1 for each modeled seismic coefficient.

The models use a pseudo-static slope stability analysis procedure to account for earthquake loading. This approach applies a static horizontal force to each element of the model based on a specified seismic coefficient to represent the destabilizing effects of seismic loading (Ling et al. 1997). We did not consider a vertical seismic loading component because the influence of a vertical component on a pseudo-static slope stability analysis is generally small for moderately steep slopes under weak to moderate ground shaking, and because the direction of force application (i.e., up or down) is not documented, nor can it be reliably predicted (Shukha and Baker 2008). The seismic coefficient represents ground motion during an earthquake, reported as a fraction of the acceleration due to gravity (g). Seismic loads are dynamic in nature; therefore, representing a maximum transient seismic load as an equivalent static load tends to overestimate the destabilizing effects of seismic loading (Damjanac and Varun 2013). This approach nevertheless allows us to explore seismic loading as a trigger mechanism.

Gusev et al. (1998) provide a record of earthquake magnitudes and ground motions for the Kamchatka peninsula between 1969 and 1993. Adjusting for small (< 10 km) epicentral distances (Fukushima and Tanaka 1990), which is consistent with an earthquake directly below the edifice, shallow ($< \sim 40$ km) earthquakes in the Kamchatka peninsula appear generally to produce peak ground accelerations (PGA) between approximately 0.05 and 0.6 g. For our analyses, we select a representative range of PGA values of 0.1–0.3 g to represent ground motions associated with moderate (M ~ 5) earthquakes. Because the pseudo-static method generally overestimates seismic loading, seismic coefficients are often taken as a fraction of the PGA. Using half of the PGA (Hynes-Griffin and Franklin 1984) to develop our pseudo-static seismic coefficients, we obtain a range of seismic coefficients of 0.05–0.15 g to be used in our models.

Given the presence of a hydrothermal system within the edifice (Belousov 1995), our models account for pore pressures in the edifice by incorporating a groundwater table at the ground surface. This simplified approach uses hydrostatic pressures, generated by the weight of groundwater, to approximate hydrothermal pressures in the subsurface. Numerical models performed by Reid (2004) suggest that local hydrothermal pressurization deep within an edifice can induce elevated pore-water pressures throughout the edifice, far from where the system is locally pressurized. As such, pore pressures significantly higher or lower than hydrostatic pressures can develop throughout the edifice. Modeling a groundwater table provides a simple approximation of pore pressures in the edifice without adding uncertainty by incorporating the complex effects of far-field hydrothermal pressures as hypothesized by Reid (2004).

We assumed a typical bulk rock unit weight of 23 kN/m^3 for all our analyses. Given that bulk rock unit weights can vary significantly based on the condition of the rock mass and the geochemical and physical composition of the intact rock, the unit weight was held constant to reduce variability in the model results associated with uncertainty in these parameters.

The residual strength of a rock mass tends to be significantly lower than its peak strength as the rock mass structure and surface conditions are disturbed during shearing (Hoek and Bray 1981; Cai et al. 2007; Reid et al. 2010). Cai et al. (2007) evaluate typical peak and residual rock mass properties for various crystalline and sedimentary rock masses, accounting for reductions in block size and surface quality, and show strength reduction equivalent to reducing the GSI of the rock mass between 45 and 65%, with the percent reduction for crystalline rocks tending toward the upper end of this range. To account for post-peak rock mass strength reduction without introducing unnecessary variability in the model behavior, we assume a constant 60% reduction in GSI from peak to residual conditions for all model cases.

This reduction is assumed to take place instantaneously in the FEM models, although in reality the reduction may take place gradually through strain softening behavior, especially for the models with lower rock mass strength (Wang et al. 2011). Because the failure surface is known to be contained within the lava domes of Young Shiveluch, the subsurface is assumed to uniformly consist of lava dome material, which reduces complexity in the model inputs and results.

Evidence of compressional, extensional, and strike-slip tectonic stress regimes in eastern Kamchatka (Heidbach et al. 2018) is likely the result of complex stress patterns associated with the junction of the Kuril-Kamchatka and Aleutian subduction zones (Seno et al. 1996). Thus, we use a horizontal-to-vertical in situ stress ratio of 1 assuming that convergence associated with subduction produces moderate horizontal stresses in the subsurface.

We do not apply a tensile strength cutoff to the rock mass strength envelope due to a lack of site-specific data. Therefore, the rock mass strength may slightly overrepresent the resistance to failure by extension.

6 Results

6.1 Geotechnical Testing

The samples from Ruapehu exhibit a wide range of porosities (3.64–30.43%), UCS values (34–258 MPa), and Young's modulus values (7–32 GPa), which allows for modeling the end-member extremes of andesite mechanical properties. The unaltered lava, Sample 1, is less porous, stronger, stiffer, and more brittle than the altered surface lava, Sample 2 (Table 1; Fig. 5). Given typical trends in porosity-strength curves in volcanic rock (e.g., Schaefer et al. 2015), the subsurface sample (Sample 3) has anomalously low strength for its porosity. This suggests that the sample has a high percentage of weak clay that has precipitated into most of the crack and pore space, in addition to the alteration of primary minerals to weaker secondary minerals [as observed for clay-dominated altered rocks in Wyering et al. (2014) and Mordensky et al. (2019)]. Although the dome material properties at depth are unknown, evidence of a hydrothermal system and extensively altered material in the debris avalanche deposits suggest that material with low porosity and low strength may exist within the edifice. Samples 1 and 2 represent upper and lower end members of the estimated ranges of possible strength values for the pre-collapse dome materials, respectively. Sample 3 represents middle-range strength values that likely represent the dome material at depth, where the failure is known to have occurred.

Table 1 Laboratory-determined porosity, uniaxial compressive strength (UCS), Hoek–Brown material constant m_i, and Young's modulus values for intact rock samples from Ruapehu

No	Sample description	Porosity (%)	UCS (MPa)	m_i	E (GPa)
1	Unaltered lava (surface)	5.59	258	33	32
2	Altered lava (surface)	30.43	34	7	7
3	Altered lava (subsurface)	3.64	92	13	18

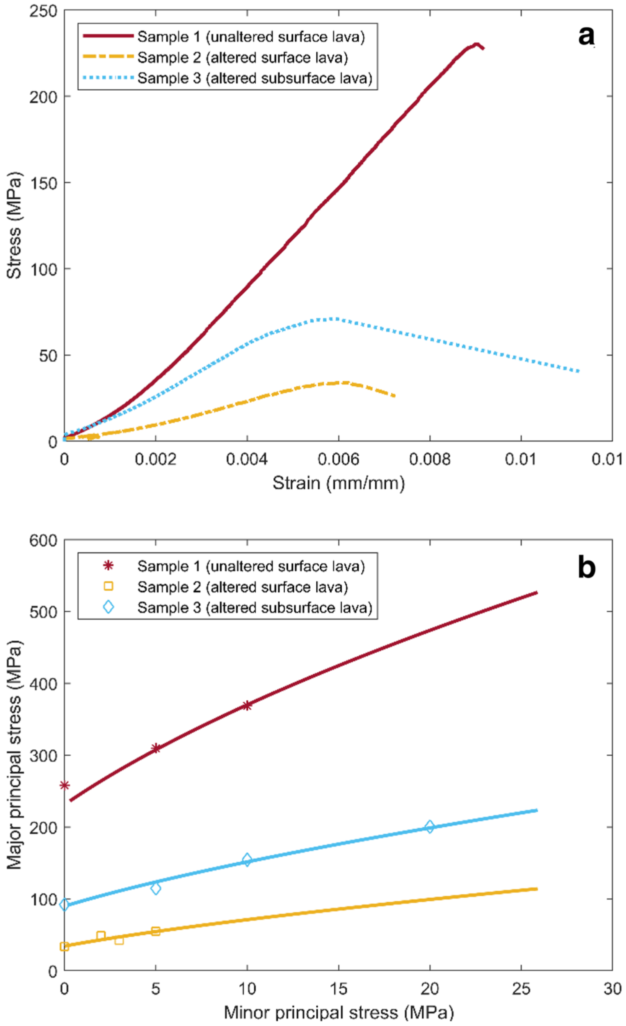

Fig. 5 Geotechnical test results. **a** Representative stress—strain curves for each block in uniaxial compression. **b** Strength envelopes for each block under various confining stresses in triaxial compression

6.2 Constraining Material Properties

We determined the back-calculated GSI values corresponding to a critical SRF of 1 for a range of seismic coefficients for each of the three tested materials (i.e., upper end member, middle range, and lower end member). Figure 6 shows GSI-seismic coefficient curves representing stability

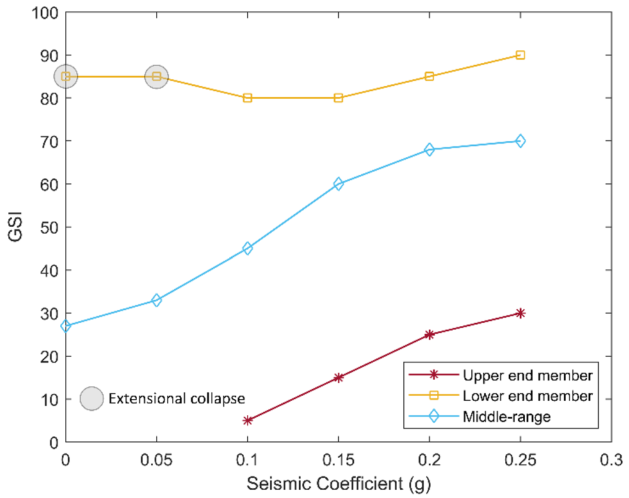

Fig. 6 Combinations of Geological Strength Index (GSI) values and seismic coefficients that produce marginally stable conditions (critical strength reduction factor ~ 1). Combinations leading to extensional collapse are highlighted by shaded circles

envelopes for each material, where points on the curves correspond to critical SRF values of approximately 1. The zones above and below each envelope represent zones of stability and instability, respectively, for each material. To better illustrate trends in the stability envelopes, Fig. 6 shows a range of seismic coefficients from 0 to 0.25 g, which extends beyond the estimated range of 0.05–0.15 g.

Model results using upper end-member intact material properties show that the dome is generally stable for seismic coefficients less than 0.1 g and requires a rock mass of very poor quality (i.e., GSI < 20) to induce failure for seismic coefficients between 0.1 and 0.15 (Fig. 6). This GSI range corresponds to a surface condition description of “very poor” to “poor” (Fig. 7). For fresh lava, discontinuity surfaces can typically be described as “good” to “very good” (Mordensky et al. 2018a). As such, GSI values less than 20 are unlikely, which suggests that the upper end-member geomechanical properties probably overestimate the true bulk dome properties.

The results also show that when the lower end-member intact material properties are considered, the dome tends

Fig. 7 Geological Strength Index (GSI) chart modified from Hoek et al. (2013) showing back-calculated ranges of GSI values from the finite element slope stability models at marginally stable (critical strength reduction factor ~ 1) conditions. Lower end-member (“Lower”) intact material properties require GSI values greater than about 80. Upper end-member (“Upper”) intact material properties correspond to GSI values less than about 20. Middle-range (“Middle”) material properties require GSI values between about 30 and 60

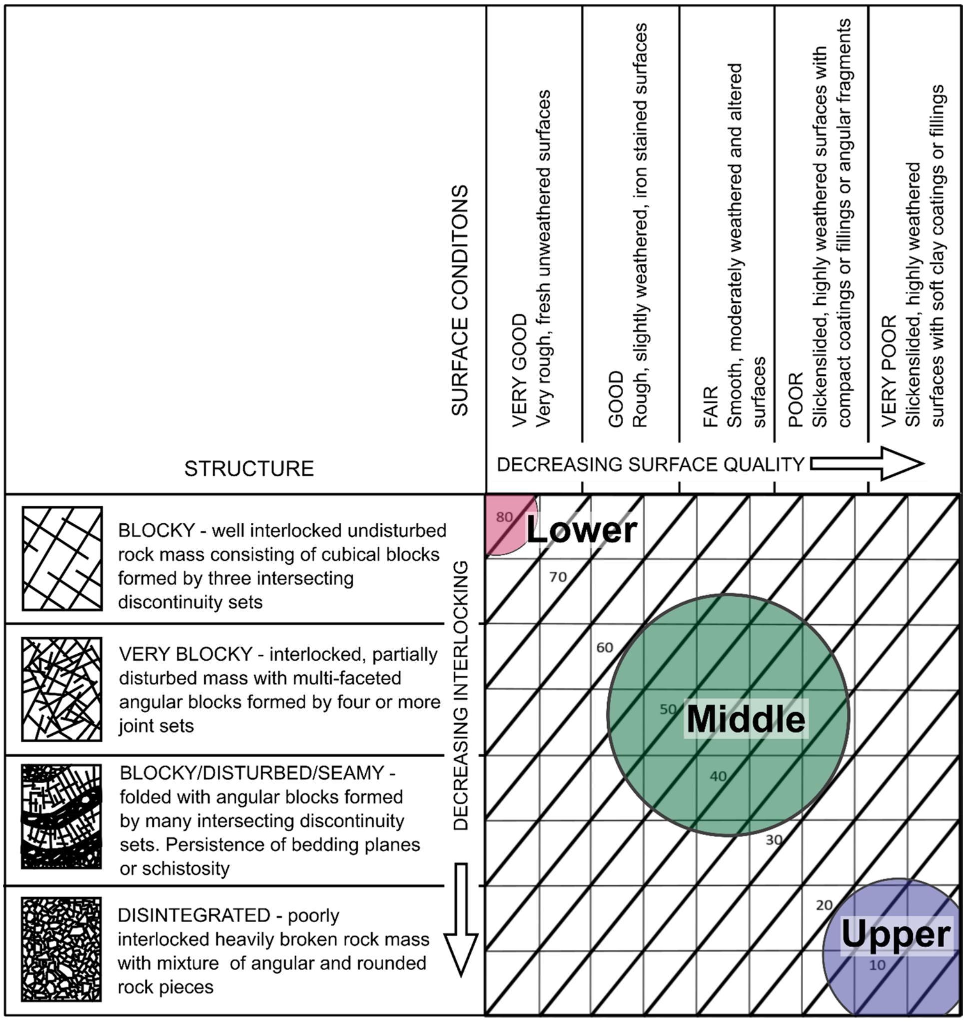

to be unstable for any GSI value less than approximately 80–85 for seismic coefficients within the expected range of 0.05–0.15 g (Fig. 6). According to Hoek et al. (2013), a GSI value of ~ 80 generally corresponds to a discontinuity surface description of "very good" (Fig. 6). Given "very poor" to "poor" discontinuity surface conditions associated with the extensive alteration of the lower end member, GSI values near 80 are highly improbable for this material. This suggests that the lower end-member geomechanical properties probably underestimate the true bulk dome properties.

For seismic coefficients within the expected range of 0.05–0.15 g, the middle-range intact material properties require GSI values between approximately 30 and 60 for marginal stability (Fig. 6). This range of GSI values corresponds to a range of discontinuity surface descriptions from "poor" to "good," which is reasonable for a rock mass consisting of variably altered andesite. Moon et al. (2005) and Heap et al. (2019a, b) suggest that GSI values for typical fractured lavas tend to fall within a range of about 50–60, and alteration tends to reduce that range by reducing surface quality (Mordensky et al. 2018a). Therefore, the range of GSI values obtained given the expected range of seismic coefficients appears to be reasonable for the pre-collapse dome materials at Young Shiveluch.

6.3 Edifice Failure Mode

Figure 8 shows the development of maximum plastic shear strain in the dome for models with middle-range intact material properties and back-calculated GSI values between 33 and 60, corresponding to seismic coefficients between 0.05 and 0.15 g. The assumed failure surface shown in Fig. 3 [based on Ponomareva et al. (1998)] is overprinted on the models shown in Fig. 8. The model results shown in Fig. 8 are at one to two strength-reduction stages past the critical SRF (i.e., the SRF is up to approximately 3% higher than the critical SRF) to show failure propagation.

For a seismic coefficient of 0.05 g and a back-calculated GSI value of 33 (Fig. 8a), strain is primarily concentrated along an extensional half-graben in the upper portion of the dome with an incipient deep-seated failure surface also developing within the dome. The deep-seated failure surface is shallower than the assumed failure surface.

For a seismic coefficient of 0.1 g and a back-calculated GSI value of 45 (Fig. 8b), strain is primarily concentrated along a deep-seated failure surface that is shallower than the assumed failure surface but has a similar shape. The toe of the modeled failure surface exits the slope at the same location as the assumed failure surface. The model results also show the development of a deeper shear band below the assumed failure surface, which suggests that failure is propagating along two deep-seated surfaces. The assumed failure surface generally aligns with the upper portion of the deeper failure surface (i.e., near the headscarp), and the lower portion of the shallower failure surface (i.e., near the toe).

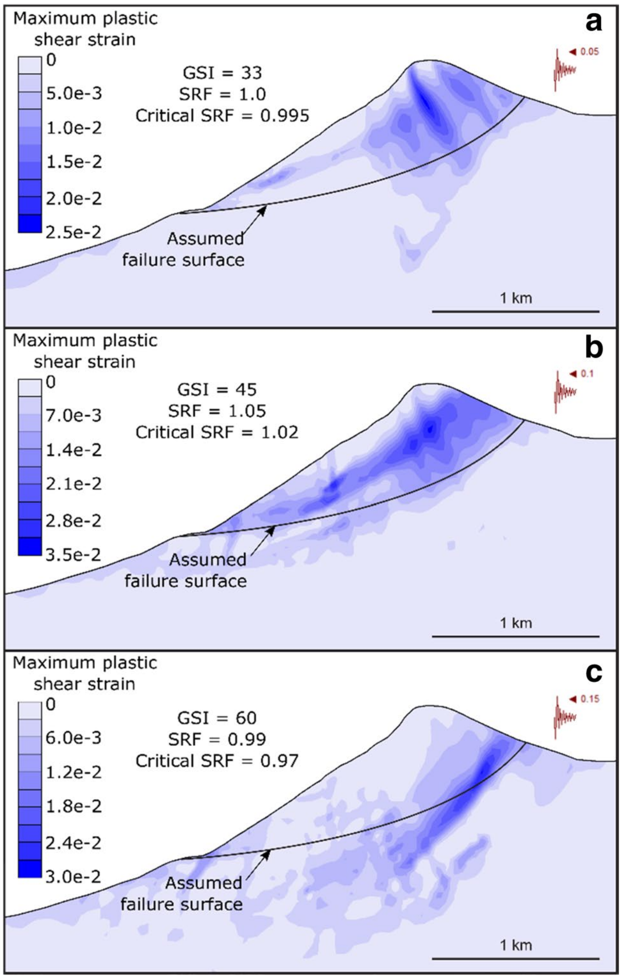

Fig. 8 Finite element slope stability model results showing concentrations of plastic shear strain in the dome at one to two stages past a critical strength reduction factor (SRF) of ~ 1, using middle-range intact material properties. **a** Seismic coefficient = 0.05 g, Geological Strength Index (GSI) = 33. **b** Seismic coefficient = 0.10 g, GSI = 45. **c** Seismic coefficient = 0.15 g, GSI = 60

For a seismic coefficient of 0.15 g and a back-calculated GSI value of 60 (Fig. 8c), strain is primarily concentrated along an extremely deep-seated failure surface, which projects significantly deeper into the edifice than the assumed failure surface. Based on the modeled shear strains, where the failure surface exits the slope is unclear.

The failure modes shown in Fig. 8a, c (extensional half-graben and extremely deep-seated shear, respectively) do not match the observed 1964 post-collapse topography (i.e., the assumed failure surface). The depth and curvature of the failure surface shown in Fig. 8b match the post-collapse topography reasonably well; therefore, this model is a better representation of the observed 1964 failure. In addition, if both the upper and lower shear bands are mobilized, a composite surface could develop, producing a geometry that very closely matches that of the 1964 collapse. Based on these results, the model presented in Fig. 8b (seismic coefficient = 0.1, GSI = 45) is our best approximation of the 1964 failure. Accordingly, we select a representative GSI value of 45 as a baseline for additional sensitivity modeling.

Figure 9 shows how the failure propagates over several stages of strength reduction analysis for the model using middle-range intact material properties, a seismic coefficient of 0.1, and a representative GSI value of 45. At a critical SRF of 1.02 (Fig. 9a), strain is concentrated along conjugate shear surfaces corresponding to maximum and minimum principal stresses in the vertical and horizontal directions, respectively. This failure mode suggests the formation of an incipient extensional graben in the upper portion of the dome. At one stage past the critical SRF (SRF = 1.03) (Fig. 9b), the failure mode begins to shift toward deep-seated rotational failure as strain concentrates in the toe of the slope. At two stages past the critical SRF (SRF = 1.05) (Fig. 9c), deep-seated rotation is the predominant failure mode (also shown in Fig. 8b).

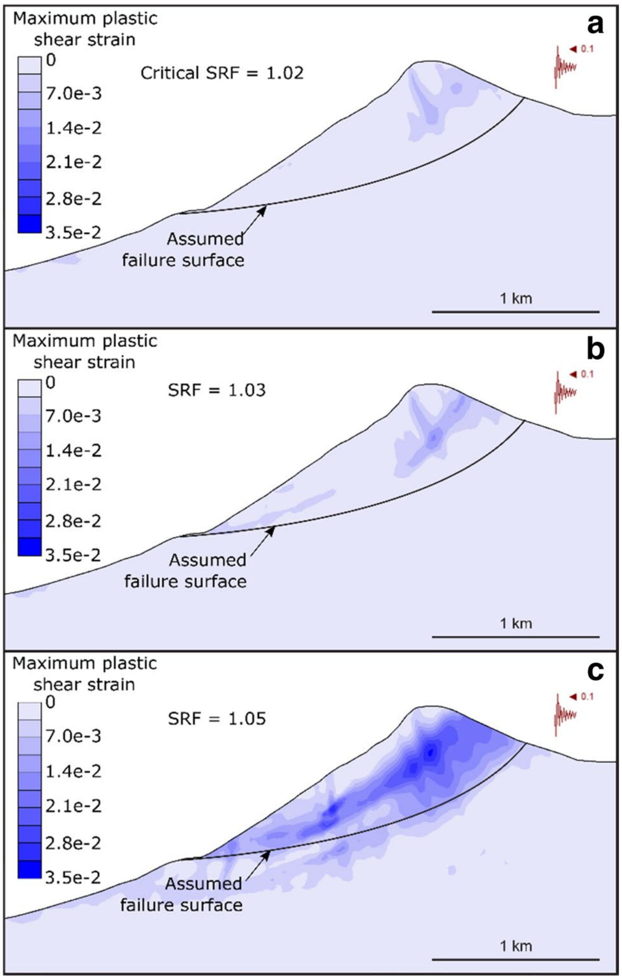

Fig. 9 Finite element slope stability model results showing development of maximum plastic shear strain in the edifice for middle-range material with a Geological Strength Index (GSI) value of 45 and a seismic coefficient of 0.1. **a** Model results at a critical strength reduction factor (SRF) of ~ 1 showing initial stage of failure under extensional collapse. **b** Model results at one stage past the critical SRF showing the failure mode in transition from extensional collapse to deep-seated rotational failure. **c** Model results at two stages past the critical SRF with shear strain concentrations showing deep-seated rotational failure as the dominant failure mode

For our simulations involving the upper end-member intact material properties, rotational failure is generally the predominant failure mode. For model cases using the lower end-member intact material properties, the failure mode is characterized by either rotational failure or extensional collapse, depending on the modeled GSI and seismic coefficient. Figure 10 shows an example of extensional collapse as the dominant failure mechanism at the critical SRF for lower end-member material using a GSI value of 85 and a seismic coefficient of 0.05. The stability envelope for the lower end-member material in Fig. 6 suggests that at marginally stable conditions (critical SRF = 1), GSI values are relatively constant over the tested range of seismic coefficients. This stability envelope differs from those of the upper end-member and middle-range materials in that the GSI required to reach marginally stable conditions does not increase with increasing seismic coefficients (Fig. 6). This appears to be associated with a change in failure mode from relatively shallow extensional collapse to deep-seated rotational failure. Figure 6 highlights the cases in which the failure mode is dominated by extensional collapse. Here, it appears that additional seismic energy is used to mobilize more material at greater depth. The physical significance of this result is limited because the lower end-member material properties used in our models are unrealistic according to the modeled back-analysis.

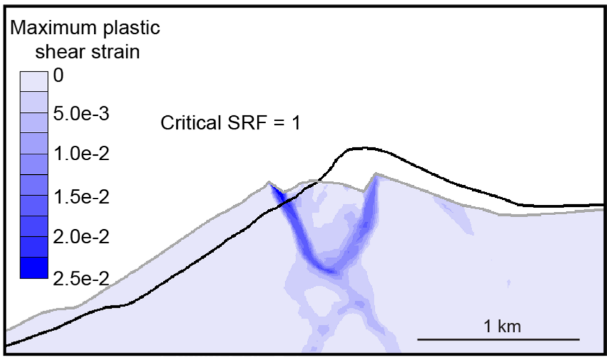

Fig. 10 Maximum plastic shear strain and deformed topography for lower end-member material with a Geological Strength Index (GSI) value of 85 and a seismic coefficient of 0.05 g at a critical strength reduction factor (SRF) of 1. Pattern of deformation illustrates that extensional collapse is the dominant failure mode under these conditions. Original topography is shown in black

6.4 Sensitivity Analysis

We performed a sensitivity analysis of the input parameters GSI, UCS, m_i, and the seismic coefficient to evaluate whether the stability of the dome is highly sensitive to changes in these parameters. Here, we varied each parameter individually relative to a baseline value to examine its influence on the critical SRF (Fig. 11). The baseline UCS and m_i values are those of the middle-range material (UCS = 92 MPa, $m_i = 13$). The baseline GSI and seismic coefficient values are those at the middle of the expected range of values for the middle-range material (GSI = 45, seismic coefficient = 0.1 g). These baseline values are the same as those used for the models shown in Figs. 8b and 9. Based on the results of the sensitivity analysis, dome stability appears to be most affected by changes in GSI. For changes in GSI up to 50%, the critical SRF changes by up to approximately 35%. The maximum change in critical SRF occurs at + 50% change in GSI; there is only an approximately 25% change in critical SRF at – 50% change in GSI. Thus, critical SRF values appear to be especially sensitive to changes in GSI when GSI is relatively high. Dome stability appears to be only moderately sensitive to changes in UCS and m_i when compared to GSI; for changes in UCS up to 50% from the baseline, the critical SRF correspondingly changes by up to 20%. Changes to the m_i parameter affect the critical SRF similarly, although we have lower confidence in this interpretation, because the results for m_i are more variable. Dome stability appears to be roughly as sensitive to changes in seismic coefficient as it is to UCS and m_i.

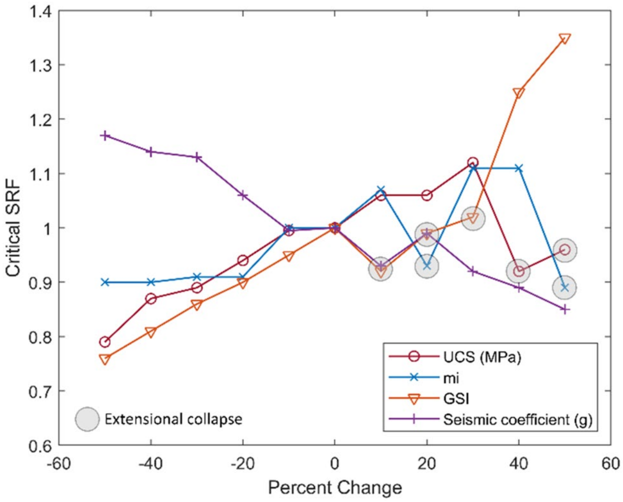

Fig. 11 Results of sensitivity analysis for Geological Strength Index (GSI), uniaxial compressive strength (UCS), the Hoek–Brown material constant m_i, and seismic coefficient. Baseline (0% change) UCS and m_i values are those of the middle-range material (UCS = 92 MPa, $m_i = 13$). Baseline GSI and seismic coefficient values are those at the middle of the back-calculated range of values for the middle-range material (GSI = 45, seismic coefficient = 0.1 g). Significant drops in GSI below the overall trends are caused by a change in failure mode from deep-seated rotation to extensional collapse (shaded circles)

For some parameter values, the sensitivity analysis shows local deviations in critical SRF values from the overall trends for UCS, m_i, and GSI. In some cases, the critical SRF values are well below the expected values according to the trends (Fig. 11). For all these cases, the dominant failure mode is extensional collapse, rather than deep-seated rotational failure. This result suggests that for the given dome geometry and the modeled ranges of input parameters, the dome is marginally stable for both failure modes, and specific combinations of input parameters tend to lead to one failure mode over the other. However, there does not appear to be a well-defined pattern of parameter combinations corresponding to changes in the failure mode.

7 Discussion

7.1 Shiveluch Dome Material Properties

The end-member intact material properties used in our models bracket possible ranges of material properties for variably altered andesite. Using these properties, the back-calculated GSI values (GSI < 20 and > 80, respectively), corresponding to marginal slope stability, are at the margins of the GSI chart (Fig. 7); thus, they are unlikely to be present given the surface conditions associated with fresh andesite lava (upper end-member) or extensively altered andesite lava (lower end-member) (Hoek et al. 2013). As such, it is unlikely that the domes at Young Shiveluch consisted entirely of either of these materials prior to the 1964 collapse. However, the intact properties of these end-member materials are not unrealistic in volcanic environments, especially those with active hydrothermal systems. del Potro and Hürlimann (2008) compile strength properties for volcanic rocks from the published literature (at least 25 sources) and provide typical ranges of UCS values for fresh and altered intact lava. Based on these literature values, the UCS of fresh lava typically ranges from about 37–342 MPa with a mean of 113 MPa, and the UCS of altered lava typically ranges from about 18–41 MPa with a mean of 30 MPa. Our upper end-member intact material (UCS = 258 MPa) lies within the upper portion of the range for fresh lava, while our lower end-member intact material (UCS = 34 MPa) is just above the mean value for altered lavas. Our middle-range material (UCS = 92 MPa) lies between the mean values for fresh and altered lavas. Thus, our selected intact materials cover an appropriate range of intact strengths for slope stability modeling of a variably altered lava dome, and it is likely that parts of the pre-collapse Shiveluch edifice could have consisted of materials similar to those tested here. Based on our model results, the overall dome materials were more likely to be similar to our middle-range material or a combination of materials with properties varying between those of the upper and lower end-member materials.

Lava domes are commonly heterogeneous, and hydrothermal systems tend to form local zones of extensive alteration surrounded by zones of more competent material within the dome (e.g., Voight 2000). Furthermore, lava within a dome can be emplaced at high temperatures and pressures, which can lead to ductile deformation in the interior of the dome while the lava is hot, subsequently affecting failure mechanisms and slope-stability thresholds (Smith et al. 2011; Heap et al. 2016; Coats et al. 2018). Accordingly, the pre-collapse domes were most likely composed of a combination of extensively altered lava, fresh lava, and intermediate material at varying temperatures and pressures. Because our slope stability models assume that the dome composition is homogeneous, the middle-range material properties probably represent a reasonable composite average of the dome material properties at Young Shiveluch at the time of the 1964 collapse.

In general, it is difficult to assign GSI values to rock masses in volcanic environments due to the heterogeneous nature of the rock and the variability in discontinuity surface quality associated with localized alteration and weathering (Apuani et al. 2005b; Moon et al. 2005; del Potro and Hürlimann 2008). Rock masses are particularly difficult to characterize at depth in active volcanic environments. Numerical models help to constrain ranges of GSI values for heterogeneous rock masses to characterize rock mass quality as a composite whole, especially when the rock mass cannot be observed directly at depth. The underlying assumption of the GSI system is that a rock mass contains sufficient randomly oriented fractures to be considered a homogeneous, isotropic continuum (Marinos and Hoek 2001). For a large (> 1 km^3) dome collapse, the scale of fractures and heterogeneities in the rock mass is very small relative to the scale of the overall slope. Based on the curvature of the post-1964 surface topography (from Ponomareva et al. 1998), which roughly coincides with the curved failure surface of the collapse (Figs. 8b, 9), the failure does not appear to be structurally controlled. This suggests that the material continuum assumption holds for this event and that the back-calculated range of GSI values for the middle-range dome materials is a valid approximation of the rock mass quality (GSI range of approximately 30–60).

7.2 Modeling Earthquake Ground Motions

Site-specific ground accelerations depend on the distance from the seismic source and the quality of the rock through which seismic energy propagates (GovindaRaju et al. 2004). The site-specific peak ground acceleration (PGA) at Young Shiveluch during the earthquake that likely triggered the 1964 collapse is unknown. We estimated a range of PGA values of 0.1–0.3 g for this event, which is representative of M ~ 5 earthquakes in Kamchatka based the records presented by Gusev et al. (1998), adjusted for small epicentral distances, consistent with a shallow earthquake under the edifice. We used seismic coefficients equal to one half of the PGA (0.05–0.15) for pseudo-static seismic slope stability analyses of the dome. Our sensitivity analysis results suggest that the stability of the dome is roughly as sensitive to changes in seismic coefficient as it is to intact material strength parameters, so this is an important factor to constrain. Using the estimated range of seismic coefficients and the middle-range material properties, the resultant range of GSI values (approximately 30–60) is reasonable for a fractured and variably altered lava dome (Moon et al. 2005). Therefore, because the modeled combinations of seismic coefficients and material properties result in failure geometry similar to the assumed failure surface (Fig. 9), we consider that the modeled seismic coefficients are a reasonable representation of the ground motions during the event.

The pseudo-static method of seismic slope stability analysis applies a static load to the model elements to represent transient seismic loading. This approach is often considered a conservative method of analysis, because the destabilizing effects of a static load are greater than those of an equivalent transient load (Damjanac and Varun 2013). We recommend future volcanic collapse studies should attempt to account for transient seismic loading in their modeling approaches (e.g., using FDM to apply dynamic seismic loads). In addition, given the importance of the magnitude of seismic loading to the model results, and to slope stability in general, it is critical to continue developing the capabilities of commercially available numerical modeling methods, such as FEM, to account for transient seismic loading using site-specific ground motion parameters.

7.3 Edifice Failure Modes

The results of our sensitivity analysis (Fig. 11) suggest that for a given set of model parameters, extensional collapse and deep-seated rotation are both possible, and that the pre-collapse Shiveluch domes may have been marginally stable with respect to both failure modes. Most of the slope stability model results show evidence of initial extensional structures such as normal faults and grabens near the crest of the dome, after which the dominant failure mode becomes rotational (Fig. 9). Models showing extensional collapse as the dominant failure mode tend to have lower factors of safety, as highlighted in Fig. 11. However, the failure surfaces for models failing by deep-seated rotation (Figs. 8b, c, 9) match the observed 1964 collapse geometry (Fig. 3) reasonably well, whereas failures resulting from extensional collapse (e.g., Fig. 10) less closely resemble the observed

1964 geometry. In many model cases, initial local extension is accompanied by incipient deep-seated rotational deformation, which ultimately dominates as failure progresses. Based on these results, we hypothesize that the 1964 dome collapse at Shiveluch may have initiated by local extensional failure, which then transformed to deep-seated rotation with the progression of failure deeper into the edifice.

Because we did not apply a tensile strength cutoff to the rock mass strength envelope, the tensile strength may be slightly overestimated in the models; as such, it is possible that the role of local extension in the dome failure models could be underrepresented. Nevertheless, local extension appears to have played an important role in the collapse.

The published literature reports several cases of lava dome collapse that have occurred through local extension and tensile rupture [e.g., Mt. Unzen, Japan (Ui et al. 1999); Santiaguito volcano, Guatemala (Hornby et al. 2019)]. Dome topography generally contributes to local extensional stress regimes, as domes tend to be oversteepened and are susceptible to outward creep as additional material is emplaced (Zorn et al. 2019). Furthermore, hydrothermal pressures within the dome can contribute to tensile fracturing in the rock mass, conditioning the dome for extensional failure (Hornby et al. 2019), although such hydrothermal pressures can also contribute to deep-seated shear failure (Reid 2004). However, we show that a seismic trigger associated with magma ascent at depth, without accompanying excess hydrothermal pressures, can also produce the deep-seated shear failure observed at Shiveluch.

Extensional structures on a broader scale can also promote large-scale edifice collapse, such as at Mount Etna (Sicily, Italy), where the southern and eastern sectors of the cone are sliding radially outward along basal weak layers, causing extension in the edifice and compression and thrusting at the bases of the flanks (Borgia et al. 1992; Murray 2019). Such large-scale extension can contribute to the formation of local extensional structures near the summit while also promoting deep-seated collapse (Borgia et al. 1992; Delcamp et al. 2008; Schaefer et al. 2013). Whether a basal weak layer (e.g., clay-rich materials or pyroclastic deposits) existed beneath the pre-collapse domes at Young Shiveluch is unclear due to a lack of site-specific evidence; however, because the model results show that extension in the edifice and deep-seated collapse is possible with a homogeneous edifice, a basal weak layer at Shiveluch is likely not necessary for the observed failure to occur.

Three-dimensional (3-D) topography in our models is represented by a two-dimensional (2-D) slope profile. As such, deformation is modeled under plane–strain and does not account for 3-D edge effects (Leshchinsky et al. 1985; Xing 1988) or the topographic effects of a radial edifice (Reid et al. 2000). In general, 2-D slope stability analyses tend to be conservative because they underestimate the factor of safety (critical SRF) when compared to 3-D analyses (Cavounidis 1987; Duncan 1996). For this reason, 2-D back-analyses of material properties commonly overestimate strength properties; thus, our back-calculated strength properties (namely GSI) may be slightly overestimated. Xing (1988) suggests that 2-D slope stability analyses become more conservative as slopes become more concave (i.e., decreasing radius of curvature) due to the increasing contribution of side resistance. Thus, a radial volcano edifice with generally convex terrain should be fairly well represented by a 2-D analysis in terms of factor of safety. Nevertheless, the modeled stability thresholds and failure modes may change when considering 3-D topographic effects. Future studies should explore whether extension in the upper edifice (i.e., graben formation), as shown in our models, occurs when accounting for 3-D topography.

7.4 Preconditioning Factors and Triggers for Collapse

The stability envelopes for the pre-collapse Shiveluch edifice shown in Fig. 6 suggest that the edifice could have collapsed without an earthquake trigger (i.e., critical SRF ~ 1 for a seismic coefficient of 0). However, for this to occur, the back-calculated GSI would need to be about 80–90 for rock masses composed of our lower end-member material and about 25–30 for rock masses composed of our middle-range material. As shown in Fig. 7, GSI values greater than 80 are highly unrealistic for our lower end-member material, so this scenario is unlikely. Similarly, GSI values of 25–30 for our middle-range material correspond to a surface quality description of “fair” to “poor” and require the rock structure to be “disturbed” to “disintegrated” (Fig. 7). This is generally very poor rock mass quality for fractured lavas. Moon et al. (2005) and Heap et al. (2019a, b) suggest that GSI values for typical fractured lavas tend to fall within a range of about 50–60. del Potro and Hürlimann (2008) cite GSI values in the published literature from about 40–85 with a mean value of about 55, and report that for the worst possible surface condition (i.e., weathered, smooth surfaces with clay infilling), the minimum possible GSI for lava is about 35. For our middle-range material, the lower bound of our back-calculated GSI range (GSI = 33) is only marginally feasible, and a GSI of less than 30 is even less feasible. Thus, the likelihood of the 1964 Shiveluch collapse occurring without an external trigger is very low.

Since the 1964 collapse, Shiveluch has experienced episodes of dome growth from 1980 to 1981, 1993–1995, and 2001–2016 (Krippner et al. 2018; Gorbach et al. 2020). Krippner et al. (2018) summarize the growth and collapse sequence for a period of relatively rapid (~ 10^5–10^6 m^3/day) dome growth that occurred between 2001 and 2013. Eight partial dome collapses occurred during this time, but they were not necessarily triggered by seismic loading. During rapid dome extrusion, lobes and spines can quickly become oversteepened and are thus highly susceptible to collpase (Voight 2000; Harnett et al. 2018; Krippner et al. 2018). Such partial collapses commonly occur without external triggers, as failure tends to be initiated by the exceedence of critical stress thresholds due to dome size or oversteepening associated with growth (Voight 2000). However, for large, deep-seated dome failures to occur, other triggering mechanisms are often necessary (Siebert 1984; Harnett et al. 2018; Elsworth et al. 2019). This is well documented in Kamchatka, where numerous large collapses have been triggerecd by internal and/or external loading, such as at Bezymianny volcano [1956 collapse triggered by cryptodome intrusion and associated seismicity (Belousov 1996; Ponomareva et al. 2006)], Kamen volcano [1.2 ka collapse triggered by earthquakes associated with the eruption of nearby Bezymianny volcano (Ponomareva et al. 2006)], and Bakening volcano [late Pleistocene and early Holocene collapses triggered by strong tectonic earthqaukes (Melekestsev et al. 1999; Ponomareva et al. 2006)].

This evidence suggests that major volcanic collpses in Kamchatka are strongly controlled by earthquakes, whereas smaller collapse events tend to be controlled by rapid dome growth and gravitational loading. However, for major deep-seated collapses to occur, edifices must also be sufficiently preconditioned for instability (i.e., through sufficient oversteepening and/or strength reduction due to internal fluid pressures) before an earthquake can trigger collapse (Voight 2000; Elsworth et al. 2019). Therefore, although moderate (M ~ 5) earthquakes occur frequently in Kamchatka [recurrence intervals of months to years (Gusev et al. 1998)], major volcanic collapses occur far less frequently [recurrence intervals of decades to centuries (Ponomareva et al. 2006)] because of the time required for preconditioning to occur. In addition, evidence of major volcanic collapses being triggered by tectonic earthquakes (e.g., Bakening volcano) suggests the 1964 Shiveluch collapse theoretically could have been triggered by a tectonic, rather than magmatic, earthquake, provided that the edifice was sufficiently preconditioned for collapse.

7.5 Implications for Volcanic Hazards

Hydrothermal alteration can contribute to volcanic instability by increasing the ratio of weaker secondary minerals to stronger primary minerals, lowering the overall strength of rocks (Reid et al. 2001; Siratovich et al. 2016; Mordensky et al. 2019). In particular, acid sulfate–argillic alteration replaces stronger minerals with weaker clays such as kaolinite and smectite, which can cause significant weakening (Reid et al. 2001; Ball et al. 2015). The influence of alteration is evident in Sample 3 used in this study, which has lower strength compared to the unaltered Sample 1 with a similar porosity. While there is very little description in the published literature of the degree, type, and pervasiveness of alteration in the pre-1964 Shiveluch domes, the active hydrothermal system at Young Shiveluch and the altered blocks in the resulting debris avalanche deposits (Belousov 1995), suggest that the dome was at least partially altered. Strength reduction associated with hydrothermal alteration thus likely played a role in its collapse susceptibility.

In addition to mineral replacement, alteration can also lead to clay mineral precipitation into cracks and pore spaces, reducing porosity and permeability and promoting pore-pressure buildup that can lead to explosive behavior (Siratovich et al. 2016; Heap et al. 2019a; Kennedy et al. 2020). Uncapping of a highly pressurized hydrothermal and/or magmatic system following dome collapse can trigger violent explosive activity, such as the phreatic eruption that followed the dome collapse at Shiveluch. In addition, the mobilization of extensively altered material in major collapse events can lead to debris avalanches that transform into cohesive lahars, which are highly mobile and can travel excessively far from their sources [e.g., Pico de Orizaba, Mexico (Carrasco-Núñez et al. 1993)]. Thus, determining the degree and extent of hydrothermally altered material is critical for assessing multi-hazard collapse events (Crowley and Zimbelman 1997; Pallister et al. 2019). Advances in spectroscopy (Kereszturi et al. 2018; Schaefer et al. 2020) and geophysical techniques (Rosas-Carbajal et al. 2016, 2017; Miller et al. 2020) allow for the identification of zones of hydrothermal alteration at the surface and at depth, which could increase the accuracy of volcanic stability assessments.

While major volcanic collapse events might occur with little warning [hours to days (Voight et al. 1999)], advance seismic monitoring (Passarelli et al. 2018; Dempsey et al. 2020) could aid in the forecasting of such events if both the state of stability of a dome is constrained (i.e., through slope stability analysis), and collapse is preceded by a period of magma or hydrothermal fluid intrusion into the edifice, as opposed to a rapid influx. This is uncommon, however, because major dome collapses often coincide with major pulses of magma extrusion (Loughlin et al. 2010).

While characterizing the physical and mechanical properties of intact rocks and rock masses in complex, dynamic volcanic environments is challenging, constraining these properties, such as through the combined use of laboratory and numerical methods used herein, is critical for the development of realistic volcanic hazard models (del Potro and Hürlimann 2008; Heap et al. 2019b). Better identification of material properties also aids in understanding the preconditioning factors and triggers of past collapses, allowing for better forward modeling of potential future collapses, the results of which can be incorporated into regional hazard and risk assessments.

8 Conclusions

The following conclusions are based on the results of our laboratory testing and finite element slope stability modeling:

1. Using our measured upper and lower end-member material properties, the required GSI values corresponding to marginal model stability lie outside the realistic range of GSI values for these rock types, which suggests that the pre-1964 dome at Shiveluch probably did not consist entirely of either of these end-member materials. Rather, the dome is best represented in our analyses by an equivalent continuum with properties closer to those of the middle-range material. Nevertheless, at the outcrop scale, the upper and lower end-member material properties are generally realistic for portions of active lava domes containing active hydrothermal systems.
2. Using the geomechanical properties of the middle-range material in our models, we found that a range of GSI values between approximately 30 and 60 appears to be a reasonable estimate for a marginally stable, variably fractured and partially altered lava dome.
3. Using a range of seismic coefficients of 0.05–0.15 g (representing ground motions expected for a M ~ 5 earthquake), the model results provide realistic back-calculated material strengths and failure geometries that match the observed failure geometry reasonably well. Therefore, we conclude that it is possible that seismic loading alone could trigger failure of a variably fractured and partially altered dome.
4. The 1964 dome collapse could have occurred by extensional collapse or deep-seated rotational failure, or a combination of both. The modeled failure surfaces associated with deep-seated rotational failure fit the observed post-failure topography better; thus, we assume that this is a good representation of the final failure mode. Local extensional failure appears to play an important role in the early development of the collapse; therefore, the development of extensional features in a dome (such as in a creeping dome) could be interpreted as increasing likelihood of failure in a subsequent triggering event.
5. Additional investigations into the complex interaction between dome structures and mechanical properties, triggering events, and failure mode, complemented by advanced numerical modeling, remote sensing, and geophysical investigations, will lead to better understanding and monitoring of collapse hazards on active volcanoes.

Acknowledgements We would like to thank Marc-André Brideau, Mark Reid, and an anonymous reviewer for their helpful reviews, and Yeh and Associates, Inc., for support during the preparation of this manuscript. We would also like to thank Gabriel Walton for providing guidance during project conception and early modeling. Any use of trade, firm, or product names is for descriptive purposes only and does not imply endorsement by the U.S. Government.

Funding No funding was received to assist with the preparation of this manuscript.

Data Availability Relevant data are provided in the manuscript.

Code Availability RS2 software is commercially available from RocScience.

Declarations

Conflict of Interest The authors declare that they have no conflicts of interest.

References

Apuani T, Corazzato C, Cancelli A, Tibaldi A (2005a) Stability of a collapsing volcano (Stromboli, Italy): limit equilibrium analysis and numerical modelling. J Volcanol Geotherm Res 144:191–210. https://doi.org/10.1016/j.jvolgeores.2004.11.028

Apuani T, Corazzato C, Cancelli A, Tibaldi A (2005b) Physical and mechanical properties of rock masses at Stromboli: a dataset for volcano instability evaluation. Bull Eng Geol Environ 64:419–431. https://doi.org/10.1007/s10064-005-0007-0

Ashwell PA, Kennedy BM, Edwards M, Cole JW (2018) Characteristics and consequences of lava dome collapse at Ruawahia, Taupo volcanic zone. New Zealand Bull Volcanol 80:43. https://doi.org/10.1007/s00445-018-1217-1

Ball JL, Stauffer PH, Calder ES, Valentine GA (2015) The hydrothermal alteration of cooling lava domes. Bull Volcanol 77:102. https://doi.org/10.1007/s00445-015-0986-z

Belousov AB (1995) The Shiveluch volcanic eruption of 12 November 1964—explosive eruption provoked by failure of the edifice. J Volcanol Geotherm Res 66:357–365. https://doi.org/10.1016/0377-0273(94)00072-O

Belousov AB (1996) Deposits of the 30 March 1956 directed blast at Bezymianny volcano, Kamchatka, Russia. Bull Volcanol 57:649–662. https://doi.org/10.1007/s004450050118

Bertuzzi R, Douglas K, Mostyn G (2016) Comparison of quantified and chart GSI for four rock masses. Eng Geol 202:24–35. https://doi.org/10.1016/j.enggeo.2016.01.002

Bishop AW (1955) The use of the slip circle in the stability analysis of slopes. Geotechnique 5:7–17. https://doi.org/10.1680/geot.1955.5.1.7

Bogoyavlenskaya GE, Braitseva OA, Melekestsev IV et al (1985) Catastrophic eruptions of the directed-blast type at Mount St. Helens, Bezymianny and Shiveluch Volcanoes. J Geodyn 3:189–218. https://doi.org/10.1016/0264-3707(85)90035-3

Borgia A, Ferrari L, Pasquarè G (1992) Importance of gravitational spreading in the tectonic and volcanic evolution of Mount Etna. Nature 357:231–235. https://doi.org/10.1038/357231a0

Cai M, Kaiser PK, Tasaka Y, Minami M (2007) Determination of residual strength parameters of jointed rock masses using the GSI system. Int J Rock Mech Min Sci 44:247–265. https://doi.org/10.1016/j.ijrmms.2006.07.005

Calder ES, Luckett R, Sparks RSJ, Voight B (2002) Mechanisms of lava dome instability and generation of rockfalls and pyroclastic flows at Soufriere Hills Volcano, Montserrat. Geol Soc London Mem 21:173–190. https://doi.org/10.1144/GSL.MEM.2002.021.01.08

Carn SA, Watts RB, Thompson G, Norton GE (2004) Anatomy of a lava dome collapse: The 20 March 2000 event at Soufrière Hills Volcano, Montserrat. J Volcanol Geotherm Res 131:241–264. https://doi.org/10.1016/S0377-0273(03)00364-0

Carr BB, Clarke AB, Vanderkluysen L (2016) The 2006 lava dome eruption of Merapi Volcano (Indonesia): detailed analysis using MODIS TIR. J Volcanol Geotherm Res 311:60–71. https://doi.org/10.1016/j.jvolgeores.2015.12.004

Carrasco-Núñez G, Vallance JW, Rose WI (1993) A voluminous avalanche-induced lahar from Citlaltépetl volcano, Mexico: implications for hazard assessment. J Volcanol Geotherm Res 59:35–46. https://doi.org/10.1016/0377-0273(93)90076-4

Cavounidis S (1987) On the ratio of factors of safety in slope stability analyses. Geotechnique 37:207–210

Coats R, Kendrick JE, Wallace PA et al (2018) Failure criteria for porous dome rocks and lavas: a study of Mt. Unzen, Japan. Solid Earth 9:1299–1328. https://doi.org/10.5194/se-9-1299-2018

Crowley JK, Zimbelman DR (1997) Mapping hydrothermally altered rocks on Mount Rainier, Washington, with Airborne visible/infrared imaging spectrometer (AVIRIS) data. Geology 25:559–562. https://doi.org/10.1130/0091-7613(1997)025%3c0559:MHAROM%3e2.3.CO;2

Damjanac B, Varun, Lorig L (2013) Seismic stability of large open pit slopes and pseudo-static analysis. 2013 Int. Symp. Slope Stab. Open Pit Min. Civ. Eng. 1203–1216

Dawson EM, Roth WH, Drescher A (1999) Slope stability analysis by strength reduction. Geotechnique 49:835–840. https://doi.org/10.1680/geot.1999.49.6.835

del Potro R, Hürlimann M (2008) Geotechnical classification and characterisation of materials for stability analyses of large volcanic slopes. Eng Geol 98:1–17. https://doi.org/10.1016/j.enggeo.2007.11.007

Delcamp A, Van de Wyk VB, James MR (2008) The influence of edifice slope and substrata on volcano spreading. J Volcanol Geotherm Res 177:925–943. https://doi.org/10.1016/j.jvolgeores.2008.07.014

Dempsey DE, Cronin SJ, Mei S, Kempa-Liehr AW (2020) Automatic precursor recognition and real-time forecasting of sudden explosive volcanic eruptions at Whakaari, New Zealand. Nat Commun 11:1–8. https://doi.org/10.1038/s41467-020-17375-2

Diefenbach AK, Bull KF, Wessels RL, McGimsey RG (2013) Photogrammetric monitoring of lava dome growth during the 2009 eruption of Redoubt Volcano. J Volcanol Geotherm Res 259:308–316. https://doi.org/10.1016/j.jvolgeores.2011.12.009

Duncan MJ (1996) State of the art: limit equilibrium and finite-element analysis of slopes. J Geotech Eng 122:577–596. https://doi.org/10.1061/(ASCE)0733-9410(1996)122:7(577)

Eberhardt E (2012) The Hoek-Brown failure criterion. Rock Mech Rock Eng 45:981–988. https://doi.org/10.1007/s00603-012-0276-4

Elsworth D, Voight B, Taron J (2019) Contemporary views of slope instability on active volcanoes. In: Volcanic Rocks: Proceedings of ISRM Workshop W2, Ponta Delgada, Azores, Portugal, 14–15 July, 2007. CRC Press

Fukushima Y, Tanaka T (1990) A new attenuation relation for peak horizontal acceleration of strong earthquake ground motion in Japan. Bull Seismol Soc Am 80:757–783. https://doi.org/10.1785/0120050138

Gorbach N, Portnyagin M, Tembrel I (2013) Volcanic structure and composition of Old Shiveluch volcano, Kamchatka. J Volcanol Geotherm Res 263:193–208. https://doi.org/10.1016/j.jvolgeores.2012.12.012

Gorbach N, Philosofova T, Portnyagin M (2020) Amphibole record of the 1964 plinian and following dome-forming eruptions of Shiveluch volcano, Kamchatka. J Volcanol Geotherm Res 407:107108. https://doi.org/10.1016/j.jvolgeores.2020.107108

Gorelchik VI, Shirokov VA, Firstov PP, Chubarova OS (1997) Shiveluch volcano: Seismicity, deep structure and forecasting eruptions (kamchatka). J Volcanol Geotherm Res 78:121–137. https://doi.org/10.1016/S0377-0273(96)00108-4

Gorshkov GS, Dubik YM (1970) Gigantic directed blast at Shiveluch volcano (Kamchatka). Bull Volcanol 34:261–288. https://doi.org/10.1007/BF02597790

GovindaRaju L, Ramana G V, HanumanthaRao C, Sitharam TG (2004) Site-specific ground response analysis. Curr Sci 1354–1362. http://www.jstor.org/stable/24109475. Accessed 1 December 2020

Gusev A, Guseva E, Petukhin A et al (1998) Peak ground accelerations in the Kamchatka Peninsula from data of strong motion instruments. Izv Phys Solid Earth 34:283–290

Hammah RE, Yacoub TE, Corkum BC, Curran JH (2005) The shear strength reduction method for the generalized Hoek-Brown criterion. In: Alaska Rocks 2005, The 40th US Symposium on Rock Mechanics (USRMS). American Rock Mechanics Association

Harnett CE, Thomas ME, Purvance MD, Neuberg J (2018) Using a discrete element approach to model lava dome emplacement and collapse. J Volcanol Geotherm Res 359:68–77. https://doi.org/10.1016/j.jvolgeores.2018.06.017

Hashiba K, Fukui K, Kataoka M (2019) Effects of water saturation on the strength and loading-rate dependence of andesite. Int J Rock Mech Min Sci 117:142–149. https://doi.org/10.1016/j.ijrmms.2019.03.023

He M, Zhang Z, Zheng J et al (2020) A new perspective on the constant mi of the Hoek-Brown failure criterion and a new model for determining the residual strength of rock. Rock Mech Rock Eng 53:3953–3967. https://doi.org/10.1007/s00603-020-02164-6

Heap MJ, Russell JK, Kennedy LA (2016) Mechanical behaviour of dacite from Mount St. Helens (USA): A link between porosity and lava dome extrusion mechanism (dome or spine)? J Volcanol Geotherm Res 328:159–177. https://doi.org/10.1016/j.jvolgeores.2016.10.015

Heap MJ, Troll VR, Kushnir ARL et al (2019a) Hydrothermal alteration of andesitic lava domes can lead to explosive volcanic behaviour. Nat Commun 10:5063. https://doi.org/10.1038/s41467-019-13102-8

Heap MJ, Villeneuve M, Albino F et al (2019b) Towards more realistic values of elastic moduli for volcano modelling. J Volcanol Geotherm Res 390:106684. https://doi.org/10.1016/j.jvolgeores.2019.106684

Heidbach O, Rajabi M, Cui X et al (2018) The World stress map database release 2016: crustal stress pattern across scales. Tectonophysics 744:484–498. https://doi.org/10.1016/j.tecto.2018.07.007

Hoek E, Bray JD (1981) Rock slope engineering. CRC Press, Boca Raton

Hoek E, Diederichs MS (2006) Empirical estimation of rock mass modulus. Int J Rock Mech Min Sci 43:203–215. https://doi.org/10.1016/j.ijrmms.2005.06.005

Hoek E, Carter TG, Diederichs MS (2013) Quantification of the geological strength index chart. In: 47th US rock mechanics/geomechanics symposium. American Rock Mechanics Association

Hornby AJ, Lavallée Y, Kendrick JE et al (2019) Brittle-ductile deformation and tensile rupture of dome lava during inflation at Santiaguito, Guatemala. J Geophys Res Solid Earth 124:10107–10131. https://doi.org/10.1029/2018JB017253

Hürlimann M, Garcia-Piera JO, Ledesma A (2000) Causes and mobility of large volcanic landslides: application to Tenerife, Canary

Islands. J Volcanol Geotherm Res 103:121–134. https://doi.org/10.1016/S0377-0273(00)00219-5

Hynes-Griffin ME, Franklin AG (1984) Rationalizing the seismic coefficient method. U.S. Department of the Army. Waterways Experiment Station. US Army Corps of Engineers, Miscellaneous Paper GL-84–13

Iverson RM (1995) Can magma-injection and groundwater forces cause massive landslides on Hawaiian volcanoes? J Volcanol Geotherm Res 66:295–308. https://doi.org/10.1016/0377-0273(94)00064-N

Kennedy BM, Farquhar A, Hilderman R et al (2020) Pressure controlled permeability in a conduit filled with fractured hydrothermal breccia reconstructed from ballistics from Whakaari (White Island), New Zealand. Geosciences 10:138. https://doi.org/10.3390/geosciences10040138

Kereszturi G, Schaefer LN, Schleiffarth WK et al (2018) Integrating airborne hyperspectral imagery and LiDAR for volcano mapping and monitoring through image classification. Int J Appl Earth Obs Geoinf 73:323–339. https://doi.org/10.1016/j.jag.2018.07.006

Krippner JB, Belousov AB, Belousova MG, Ramsey MS (2018) Parametric analysis of lava dome-collapse events and pyroclastic deposits at Shiveluch volcano, Kamchatka, using visible and infrared satellite data. J Volcanol Geotherm Res 354:115–129. https://doi.org/10.1016/J.JVOLGEORES.2018.01.027

Lavallée Y, Kendrick JE (2021) A review of the physical and mechanical properties of volcanic rocks and magmas in the brittle and ductile regimes. Forecast Plan Volcan Hazards Risks Disasters 2:153–238. https://doi.org/10.1016/B978-0-12-818082-2.00005-6

Leshchinsky D, Baker R, Silver ML (1985) Three dimensional analysis of slope stability. Int J Numer Anal Methods Geomech 9:199–223. https://doi.org/10.1002/nag.1610090302

Ling HI, Leshchinsky D, Mohri Y (1997) Soil slopes under combined horizontal and vertical seismic accelerations. Earthq Eng Struct Dyn 26:1231–1241. https://doi.org/10.1002/(SICI)1096-9845(199712)26:12%3c1231::AID-EQE707%3e3.0.CO;2-Z

Lipman PW, Moore JG, Swanson DA (1981) Bulging of the north flank before the May 18 eruption: Geodetic data. US Geol Surv Prof Pap 1250:143–155

Loughlin SC, Luckett R, Ryan G et al (2010) An overview of lava dome evolution, dome collapse and cyclicity at Soufrière Hills Volcano, Montserrat, 2005–2007. Geophys Res Lett 37:L00E16. https://doi.org/10.1029/2010GL042547

Marinos P, Hoek E (2001) Estimating the geotechnical properties of heterogeneous rock masses such as flysch. Bull Eng Geol Environ 60:85–92. https://doi.org/10.1007/s100640000090

Melekestsev IV, Dirksen OV, Girina OA (1999) A giant landslide-explosion circue and debris avalanche at Bakening volcano, Kamchatka. Volcanol Seismol 20:265–279

Miller CA, Schaefer LN, Kereszturi G, Fournier D (2020) Three-dimensional mapping of Mt. Ruapehu volcano, New Zealand, from aeromagnetic data inversion and hyperspectral imaging. J Geophys Res Solid Earth 125:2019JB018247. https://doi.org/10.1029/2019JB018247

Moon V, Bradshaw J, Smith R, de Lange W (2005) Geotechnical characterisation of stratocone crater wall sequences, White Island Volcano, New Zealand. Eng Geol 81:146–178. https://doi.org/10.1016/j.enggeo.2005.07.014

Mordensky SP, Villeneuve MC, Farquharson JI et al (2018a) Rock mass properties and edifice strength data from Pinnacle Ridge, Mt. Ruapehu, New Zealand. J Volcanol Geotherm Res 367:46–62. https://doi.org/10.1016/j.jvolgeores.2018.09.012

Mordensky SP, Villeneuve MC, Kennedy BM et al (2018b) Physical and mechanical property relationships of a shallow intrusion and volcanic host rock, Pinnacle Ridge, Mt. Ruapehu, New Zealand. J Volcanol Geotherm Res 359:1–20. https://doi.org/10.1016/j.jvolgeores.2018.05.020

Mordensky SP, Heap MJ, Kennedy BM et al (2019) Influence of alteration on the mechanical behaviour and failure mode of andesite: implications for shallow seismicity and volcano monitoring. Bull Volcanol 81:44. https://doi.org/10.1007/s00445-019-1306-9

Murray JB (2019) The cryptic summit graben of Mt Etna Volcano. J Volcanol Geotherm Res 387:106657. https://doi.org/10.1016/j.jvolgeores.2019.07.024

Pallister J, Wessels R, Griswold J et al (2019) Monitoring, forecasting collapse events, and mapping pyroclastic deposits at Sinabung volcano with satellite imagery. J Volcanol Geotherm Res 382:149–163. https://doi.org/10.1016/j.jvolgeores.2018.05.012

Passarelli L, Heryandoko N, Cesca S et al (2018) Magmatic or not magmatic? The 2015–2016 seismic swarm at the long-dormant Jailolo volcano, West Halmahera. Indonesia Front Earth Sci 6:79. https://doi.org/10.3389/feart.2018.00079

Ponomareva V, Pevzner M, Melekestsev I (1998) Large debris avalanches and associated eruptions in the Holocene eruptive history of Shiveluch Volcano, Kamchatka, Russia. Bull Volcanol 59:490–505. https://doi.org/10.1007/s004450050206

Ponomareva VV, Melekestsev IV, Dirksen OV (2006) Sector collapses and large landslides on late Pleistocene-Holocene volcanoes in Kamchatka, Russia. J Volcanol Geotherm Res 158:117–138. https://doi.org/10.1016/j.jvolgeores.2006.04.016

Ponomareva V, Kyle P, Pevzner M et al (2007) Holocene eruptive history of Shiveluch Volcano, Kamchatka Peninsula, Russia. In: Eichelberger J, Gordeev E, Izbekov P et al (eds) Volcanism and subduction: the Kamchatka region. American Geophysical Union, Washington, D.C., pp 263–282

Reid ME (2004) Massive collapse of volcano edifices triggered by hydrothermal pressurization. Geology 32:373–376. https://doi.org/10.1130/G20300.1

Reid ME, Christian SB, Brien DL (2000) Gravitational stability of three-dimensional stratovolcano edifices. J Geophys Res Solid Earth 105:6043–6056. https://doi.org/10.1029/1999JB900310

Reid ME, Sisson TW, Brien DL (2001) Volcano collapse promoted by hydrothermal alteration and edifice shape, Mount Rainier, Washington. Geology 29:779–782. https://doi.org/10.1130/0091-7613(2001)029%3c0779:VCPBHA%3e2.0.CO;2

Reid ME, Keith TEC, Kayen RE et al (2010) Volcano collapse promoted by progressive strength reduction: new data from Mount St Helens. Bull Volcanol 72:761–766. https://doi.org/10.1007/s00445-010-0377-4

RocScience (2019a) RocData v 5.0. RocScience Inc. Toronto, Canada.

RocScience (2019b) RS2 v 10.0. RocScience Inc. Toronto, Canada.

Rosas-Carbajal M, Komorowski J-C, Nicollin F, Gibert D (2016) Volcano electrical tomography unveils edifice collapse hazard linked to hydrothermal system structure and dynamics. Sci Rep 6:29899. https://doi.org/10.1038/srep29899

Rosas-Carbajal M, Jourde K, Marteau J et al (2017) Three-dimensional density structure of La Soufrière de Guadeloupe lava dome from simultaneous muon radiographies and gravity data. Geophys Res Lett 44:6743–6751. https://doi.org/10.1002/2017GL074285

Sari M (2010) A simple approximation to estimate the Hoek-Brown parameter ‘mi’for intact rocks. In: Zhao J, Labiouse V, Dudt J, Mathier J (eds) Rock mechanics in civil and environmental engineering. Taylor and Francis Group, London, pp 169–172

Schaefer LN, Oommen T, Corazzato C et al (2013) An integrated field-numerical approach to assess slope stability hazards at volcanoes: the example of Pacaya. Guatemala Bull Volcanol 75:720. https://doi.org/10.1007/s00445-013-0720-7

Schaefer LN, Kendrick JE, Lavallée Y et al (2015) Geomechanical rock properties of a basaltic volcano. Name Front Earth Sci 3:29. https://doi.org/10.3389/feart.2015.00029

Schaefer LN, Kennedy BM, Villeneuve MC et al (2018) Stability assessment of the Crater Lake/Te Wai-ā-moe overflow channel at Mt. Ruapehu (New Zealand), and implications for volcanic lake break-out triggers. J Volcanol Geotherm Res 358:31–44. https://doi.org/10.1016/j.jvolgeores.2018.06.011

Schaefer LN, Kereszturi G, Villeneuve MC, Kennedy BK (2020) Towards correlating physical and mechanical volcanic rock with infrared spectroscopy: Understanding the influence of weathering and hydrothermal alteration. In: Proceedings of the 54th US Rock Mechanics/Geomechanics Symposium. American Rock Mechanics Association, Golden, CO

Seno T, Sakurai T, Stein S (1996) Can the Okhotsk plate be discriminated from the North American plate? J Geophys Res Solid Earth 101:11305–11315. https://doi.org/10.1029/96JB00532

Shukha R, Baker R (2008) Design implications of the vertical pseudo-static coefficient in slope analysis. Comput Geotech 35:86–96. https://doi.org/10.1016/j.compgeo.2007.01.005

Siebert L (1984) Large volcanic debris avalanches: Characteristics of source areas, deposits, and associated eruptions. J Volcanol Geotherm Res 22:163–197. https://doi.org/10.1016/0377-0273(84)90002-7

Siratovich PA, Heap MJ, Villeneuve MC et al (2016) Mechanical behaviour of the Rotokawa Andesites (New Zealand): insight into permeability evolution and stress-induced behaviour in an actively utilised geothermal reservoir. Geothermics 64:163–179. https://doi.org/10.1016/j.geothermics.2016.05.005

Sitharam TG, Sridevi J, Shimizu N (2001) Practical equivalent continuum characterization of jointed rock masses. Int J Rock Mech Min Sci 38:437–448. https://doi.org/10.1016/S1365-1609(01)00010-7

Smith R, Sammonds PR, Tuffen H, Meredith PG (2011) Evolution of the mechanics of the 2004–2008 Mt. St. Helens lava dome with time and temperature. Earth Planet Sci Lett 307:191–200. https://doi.org/10.1016/j.epsl.2011.04.044

Sousa J, Voight B (1995) Multiple-pulsed debris avalanche emplacement at Mount St. Helens in 1980: evidence from numerical continuum flow simulations. J Volcanol Geotherm Res 66:227–250. https://doi.org/10.1016/0377-0273(94)00067-Q

Ui T, Matsuwo N, Sumita M, Fujinawa A (1999) Generation of block and ash flows during the 1990–1995 eruption of Unzen Volcano, Japan. J Volcanol Geotherm Res 89:123–137. https://doi.org/10.1016/S0377-0273(98)00128-0

Voight B (2000) Structural stability of andesite volcanoes and lava domes. Philos Trans R Soc London 358:1663–1703. https://doi.org/10.1098/rsta.2000.0609

Voight B, Elsworth D (2000) Instability and collapse of hazardous gas-pressurized lava domes. Geophys Res Lett 27:1–4. https://doi.org/10.1029/1999GL008389

Voight B, Janda RJ, Glicken H (1983) Nature and mechanics of the mount St Helens rockslide-avalanche of 18 May 1980. Geotechnique 20:243–273. https://doi.org/10.1016/0148-9062(83)90666-6

Voight B, Sparks RSJ, Miller AD et al (1999) Magma flow instability and cyclic activity at Soufriere Hills volcano, Montserrat, British West Indies. Science 283:1138–1142. https://doi.org/10.1126/science.283.5405.1138

Wang S, Zheng H, Li C, Ge X (2011) A finite element implementation of strain-softening rock mass. Int J Rock Mech Min Sci 48:67–76. https://doi.org/10.1016/j.ijrmms.2010.11.001

Wong LNY, Maruvanchery V, Liu G (2016) Water effects on rock strength and stiffness degradation. Acta Geotech 11:713–737. https://doi.org/10.1007/s11440-015-0407-7

Wyering LD, Villeneuve MC, Wallis IC et al (2014) Mechanical and physical properties of hydrothermally altered rocks, Taupo volcanic zone, New Zealand. J Volcanol Geotherm Res 288:76–93. https://doi.org/10.1016/j.jvolgeores.2014.10.008

Xing Z (1988) Three-dimensional stability analysis of concave slopes in plan view. J Geotech Eng 114:658–671. https://doi.org/10.1061/(ASCE)0733-9410(1988)114:6(658)

Zorn EU, Le Corvec N, Varley NR et al (2019) Load stress controls on directional lava dome growth at Volcán de Colima, Mexico. Front Earth Sci 7:1–18. https://doi.org/10.3389/feart.2019.00084